J Mater Sci: Mater Electron (2022) 33:18039–18053

Dark and illuminated electrical characteristics of Schottky device with Zn-complex interface layer

S. Karadeniz[1], D. E. Yıldız[2,*] 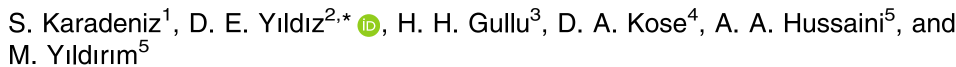, H. H. Gullu[3], D. A. Kose[4], A. A. Hussaini[5], and M. Yıldırım[5]

[1] *Department of Energy Systems Engineering, Faculty of Engineering, Giresun University, 28000 Giresun, Turkey*
[2] *Department of Physics, Faculty of Arts and Sciences, Hitit University, 19030 Çorum, Turkey*
[3] *Microelectronics, Guidance and Electro-Optics Division, Optical and Optomechanical Design Department, ASELSAN Inc., 06200 Ankara, Turkey*
[4] *Department of Chemistry, Faculty of Arts and Sciences, Hitit University, 19030 Çorum, Turkey*
[5] *Department of Biotechnology, Faculty of Science, Selcuk University, 42030 Konya, Turkey*

Received: 25 April 2022
Accepted: 25 June 2022
Published online: 18 July 2022

© The Author(s), under exclusive licence to Springer Science+Business Media, LLC, part of Springer Nature 2022

ABSTRACT

In this study, metal/Zn-complex/semiconductor (MPS) Schottky photodiodes are fabricated. Interface layer is deposited using a metal-nicotinate/nicotinamide mixed ligand $[Zn(C_6H_6N_2O)_2(C_6H_4NO_2)_2(H_2O)]\cdot 1/2(H_2O)$ complex synthesized with Zn dopant. Different film layers are obtained by dissolving 0.5, 1.0, 2.0, and 3.0 mg Zn-complex in 1 mg spin-coating solution. Thermal analysis techniques are performed between room temperature and 900 °C to study the thermal behavior of the complex as a metal oxide. The surface morphology of the polymeric film layers is investigated by microscopy methods, and the results show relatively smooth and compact surface characteristics for all Zn-complex mass contributions. To evaluate electrical properties of the fabricated device, current–voltage, capacitance–voltage and conductance–voltage measurements are performed under dark and illumination intensities between 20 and 100 mW/cm^2 depending on Zn-complex mass at the interface. These measurements indicate light sensitivity of the diodes. In addition, transient characteristics are investigated at these illumination intensities to evaluate photoresponse behaviors. Then, the highest photoconductivity is recorded for 3 mg Zn-complex. The experimental results indicate that the diodes exhibit good photosensitive behavior, and they can be used for opto-electronic applications.

Address correspondence to E-mail: desrayildiz@hitit.edu.tr

https://doi.org/10.1007/s10854-022-08664-1

1 Introduction

Metal/semiconductor (MS) contacts are of great interest due to their long-term use in electronic devices such as diodes, transistors, and capacitors [1–3]. These structures act as a rectifier and they allow charge carriers to transmit under forward bias and limit their motion under reverse bias [4]. They are also evaluated as a capacitor that they store charge and energy at the MS interface [5]. The presence of a thin film layer between metal and semiconductor layers transforms the corresponding device into a metal/insulator/semiconductor (MIS) or metal/oxide/semiconductor (MOS) diode structure [6, 7]. These structures are important research tools for characterizing new interface and also semiconductor materials. In addition, manufacturing of them plays significant role in fabrication of some useful technological devices such as photodiode and photodetector [8].

In recent years, research on this type of diodes is focused on organic interface layers to increase the performance of MS structures. In this context, optoelectronic devices with superior optical and electrical properties are produced by using organic/polymer materials at the interface [9, 10]. Because of light weight, mechanical strength and optical properties, the polymeric materials have a wide range of applications and they attract great attention in both academic and industrial research areas [11–14]. The usage area of these materials is not limited with MS device, but also they can be found in solar cells and light-emitting diode applications [15, 16]. However, the key point in production of a high-quality Schottky diode is deposition of a suitable polymer interfacial layer at MS interface.

Polymers are suitable materials for metal/polymer/semiconductor (MPS) Schottky structures and some of them widely used in literature can be listed as poly (vinyl alcohol) (PVA), poly (ethane), polyaniline (PANI), and polypyrrole (PPy). For this reason, polymers and their derivatives are used as interfacial materials due to their suitability for nanosize fabrication and their high surface-area-to-volume ratio [17–23]. These materials can also provide advantages on the device characteristics by increasing number of charge carriers [24, 25].

Furthermore, a device becomes more sensitive to illumination intensities in the presence of a polymeric interface layer. It is because device performance and long-term stability depend on controlled-charge transmission of the interfacial layer [26, 27]. Many intrinsic charge carriers are not located within the organic polymer layer. Pure polymers are in poor conductivity and it is necessary to provide additional charge carriers by doping to improve p- or n-type conductivity behavior. When a polymer is doped, changes may occur in both its molecular structure and microstructural properties. Today, many researchers examine electrical properties of the polymers doped with metal ions [28–30]. When a metal-doped polymer is used as an interfacial layer, it provides better electrical and optical results in MPS devices [31].

At this point, Zn is a dopant material with high electron mobility that can be contributed to the interface layer in Si-based MPS structures. The wide bandgap and corrosion resistance of its compounds are some of leading features and make it popular in electronic applications. Thus, Zn-containing compounds such as zinc oxide (ZnO), zinc sulfide ($ZnSO_4$), and zinc chloride ($ZnCl_2$) are used in thin film transistors, gas detectors, photodetectors, and many other applications [32–34].

Photodetectors are known as devices that can detect light and convert it into electrical signals [35]. For over two decades, scientists focus on improving the light-sensing properties of MS devices [36–38]. In these works, many inorganic, organic, and polymer materials are used to improve photon detection properties of such devices [39–41]. Thus, metal oxides or polymers can be preferred as interface layer in order to produce high-performance photodiode devices, and also to control their electrical properties [37, 42, 43].

In this work, the fabrication and characterization of a polymeric Si-based photodetector is reported. Therefore, Zn-doped nicotinate/nicotinamide mixed ligand complex is spin-coated on n-type Si substrate to form a photodiode. Electrical and opto-electronic properties of the prepared photodiodes are investigated by current–voltage ($I-V$), capacitance–voltage ($C-V$), conductance–voltage ($G-V$), and transient photoconductivity measurements under distinct illumination intensity in ambient temperature.

2 Experimental details

2.1 Synthesis

Nicotinic acid ($C_6H_5NO_2$), nicotinamide ($C_6H_6N_2O$), natrium bicarbonate ($NaHCO_3$), and zinc acetate ($Zn(CH_3COO)_2{\cdot}2H_2O$) are obtained from the Sigma-Aldrich company and they are used in the synthesis of the Zn-complexes, $[Zn(C_6H_6N_2O)_2(C_6H_4NO_2)_2(H_2O)]\ 1/2(H_2O)$. First, to increase the solubility of the $C_6H_5NO_2$ molecule in water, the molecule is converted into sodium salt (Fig. 1a). For this, 0.02 mol (2.462 g) of $C_6H_5NO_2$ is taken into 50 mL of distilled water and 0.02 mol of $NaHCO_3$ (1.68 g) is slowly added to the solution as a solid to prevent foaming. When adding suddenly, the solution may overflow with the suddenly (or immediately) release of CO_2. Firstly, 0.02 mol (2.442 g) solution of $C_6H_6N_2O$ molecule, which is the other neutral ligand, is prepared in 50 ml of purified water, and added onto the nicotinate ligand which is converted into sodium salt. The resulting solution is mixed in a magnetic stirrer for 30 min to provide homogeneity. Finally, the acetate salt of the Zn(II) cation, which would act as the coordination center, is slowly added to the reaction vessel as 0.01 mol (2.195 g) solid (Fig. 1b). The resulting total solution is stirred at 60 °C on a magnetic stirrer hot-plate for 5 h. The diminished solvent of the solution is preserved by adding not more than 100 mL in total. There are two main purposes of mixing by heating. At first, it can support crystallization process in the total solution at room temperature and then helps to react it easily at a temperature above room temperature. Additionally, it is used to ensure that the reaction residue acetic acid (CH_3COOH), which may have a very low pH increasing feature as a contaminant, is removed from the environment as much as possible [44–46]. The beaker into which the last solution transferred is sealed with paraffin for holes and left to stand until crystal formed. The white acicular crystals formed after about 10–15 days are collected and stored for structural analysis.

Chemical composition analysis for the synthesized complex compound confirms the proposed molecular formula. According to this, the chemical composition data of complex is C: 47.84%, H: 3.85%, and N: 14.13% for experimental and C: 48.09%, H: 4.18%, and N: 14.03% for calculated chemical composition, respectively.

2.2 Device fabrication and characterization

The fabrication processes of photodiodes are started by cleaning of the n-Si wafer, which has (100) crystal orientation, 1–20 Ω.cm resistivity and 300 μm thickness, and it is used as substrate and semiconductor material. Initially, the wafer is divided to 2 cm^2

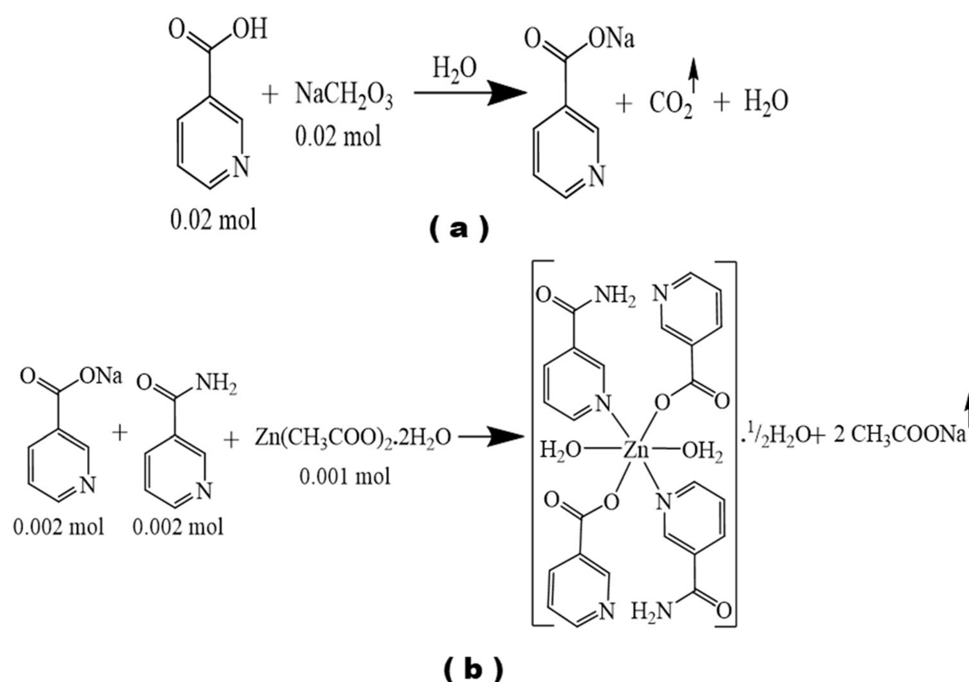

Fig. 1 Equations of metal-nicotinic acid/nicotinamide complex synthesis

square pieces and they are cleaned by ultrasonic cleaner in acetone, distilled water and isopropanol in 30 min for each step. Then, the wafer pieces are immerged into $HF:H_2O$ (1:10) solution for 30 s to remove native oxide layers from the wafer surfaces. After cleaning process, gold (Au) metal with purity of 99.99% is evaporated onto the back surface of Si substrates at the pressure of 2×10^{-5} Torr, 150-nm-thick layer is obtained by using a thermal evaporation system. Followed by evaporation step, post-annealing process is carried out at 500 °C for 5 min in dry nitrogen (N_2) atmosphere. It is applied to form a heavily doped epilayer with the same doping type (n^+) as substrate to reduce the barrier width of Au/n-Si back contact. The obtained Zn-doped nicotinate/nicotinamide mixed ligand complex is coated on the front polished wafer surfaces by spin-coating technique at 3000 rpm and in 30 s. 0.5, 1.0, 2.0, and 3.0 mg Zn-complex dissolved in de-ionized water and the final solution is obtained with a mass of 1 mg. The solutions with different contribution rates of Zn-complex are used to obtain interlayer different in molarities of Zn-complex material at Au/n-Si devices. In order to evaporate water used in solvent layers, the coated wafers are heated on a heater at 80 °C. After this process, the obtained spin-coated 0.5 mg Zn-complex/n-Si, 1 mg Zn-complex/n-Si, 2 mg Zn-complex /n-Si, and 3 mg Zn-complex/n-Si are transferred to the thermal evaporator chamber for rectifier contact coating. To reduce absorption loss, 100-nm-thick Au rectifying electrode is coated on the top of the Zn-complex film.

The schematic representation of the fabricated diode is presented in Fig. 2. Thermal analysis techniques are carried out between the temperatures of ambient and 900 °C where the Zn-complex is in ZnO form coated as the interface layer. These surface properties of doped films are examined using atomic force microscope (AFM) and scanning electron microscope (SEM). $I-V$ measurements of the fabricated device are performed under dark and distinct illumination intensities (from 20 to 100 mW/cm^2) at room temperature for voltage range of − 5 to + 5 V using a 1.5AM filter solar simulator. The $C-V$ and $G-V$ measurements are carried out in a wide frequency range (1 kHz-1000 kHz) at room temperature under dark environment. The response time is measured under the reverse bias of − 3 V.

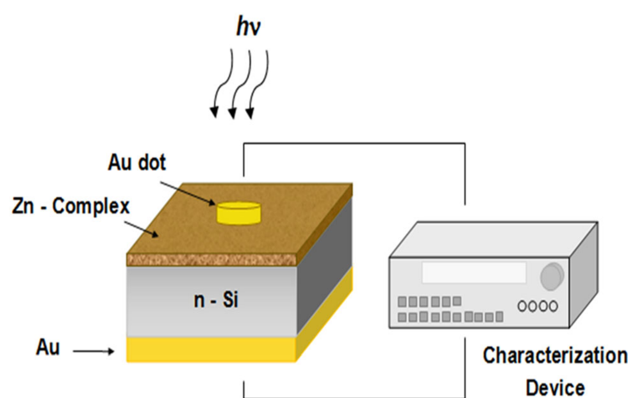

Fig. 2 Schematic representation of fabricated diode with connection to the electrical measurement set-up

3 Results and discussion

Thermal analysis curves of the coordination compound with mixed ligands of the Zn metal cation containing $C_6H_5NO_2/C_6H_6N_2O$ ligands are presented in Fig. 3a. The data related to the degradation steps and degradation products are also given in Table 1. The first decomposition step of the complex compound consists of removal of 1/2 mol of hydrate water and 2 mol of crystal water coordinating the metal cation (exp. 7.21%; calc. 7.51%). It is observed that the organic ligands begin to degrade in the next decomposition step of the complex compound, which becomes dehydrated. In this step, it is determined that 2 mol of $C_6H_6N_2O$ ligand, which provide coordination to the monodentate through the pyridine nitrogen atom as neutrally to the metal cation, and 1 mol of nicotinic acid ligand are removed. In the temperature range of 547–897 °C, decomposition of the complex is completed. In this step, all of 2 mol of $C_6H_5NO_2$, that is coordinated through the acidic oxygen atom as monoanionic-monodentate, are burnt remaining in the structure. After combustion of the complex is completed, it is confirmed by the powder X-ray diffraction (XRD) pattern that the residue ZnO remained as a final degradation product. Compatibility of the experimental (15.03%) and theoretical (13.59%) residue percentage amounts of the relevant degradation residue also supports the claim for this work. The experimental residue percentage is lower than the theoretical residue percentage, and this result can be explained by the fact that complete combustion cannot occur due to the lack of sufficient oxygen in the thermal analysis performed in N_2 atmosphere. Since there is no completed combustion,

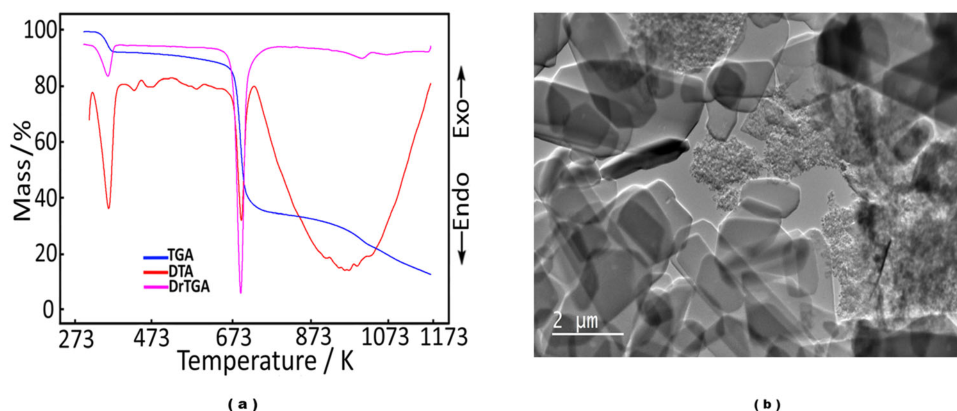

Fig. 3 **a** TG-DTG and DTA plots and **b** SEM image of prepared $[Zn(C_6H_6N_2O)_2(C_6H_4NO_2)_2(H_2O)]\cdot1/2(H_2O)$ complex

Table 1 Thermal analysis data of metal-nicotinate/nicotinamide mixed ligand complex

Complexes		Temp. range (°C)	DTA_{max} (°C)	Removed groups	Mass loss (%)		Remain product (%)		Decomp. product	Color
					Exp	Calc	Exp	Calc		
$[Zn(C_6H_6N_2O)_2(C_6H_4NO_2)_2(H_2O)]\cdot1/2(H_2O)$										White
$C_{24}H_{25}N_6O_{8.5}Zn$	1	70–150	95	2.5 H_2O	7.21	7.51				
598.87 g/mol	2	163–541	− 176;315;426	$2C_6H_6N_2O$ $C_6H_6N_2O$	53.23	53.83				
	3	351–887	696	$C_5H_4NO_2$ CHO	24.53	25.07	15.03	13.59	ZnO	Black

some carbon residue accumulates on the metal oxide as carbonized. The fact that the color of the final residue product is black, while white color is expected, supports this situation. SEM technique is employed for morphology and distribution of the obtained $[Zn(C_6H_6N_2O)_2(C_6H_4NO_2)_2(H_2O)]\cdot1/2(H_2O)$ complex on the interface layer, and SEM image is shown in Fig. 3b. According to this image, Zn-doped films consist of flake like structures with a high degree of similarity and uniformity. These structures are formed cascaded arrangement with an orderly manner.

Figure 4a–d shows AFM images of the $[Zn(C_6H_6N_2O)_2(C_6H_4NO_2)_2(H_2O)]\cdot1/2(H_2O)$ complex with effects of the Zn dopant. AFM images are obtained in non-contact mode at room temperature. It is observed from all images that grain size formation is achieved for all samples. On the other hand, grains are approximately equal in size and well coated on the surface. As a result, relatively smooth and compact surfaces are obtained. In addition, the films are in low porosity and uniformly distributed on the Si surface. Average surface roughness of these films for doping level of 0.5 mg Zn-complex, 1 mg Zn-complex, 2 mg Zn-complex and 3 mg Zn-complex are found as to be 1.53, 1.72, 1.78, and 2.57 nm, respectively. AFM results show that the amount of Zn changes the surface roughness where there is an increase in these values with increasing Zn contribution. This kind of change can also affect the photoresponse and photoelectric characteristics of device. Additionally, average height of flakes for these complex films is determined as about 18.05 nm.

Figure 5a–d demonstrates experimental forward and reverse bias $I-V$ plots of Au/Zn-complex/n-Si/Au photodiodes with various Zn-complex contents under dark and different light intensities. Since $I-V$ measurement is an important tool and conventional step to understand the electrical properties of the diodes, using these measurements, it is possible to obtain main performance parameters as diode ideality factor (n), barrier height (Φ_B), and saturation current (I_0). As seen from Fig. 5, all fabricated devices exhibit a rectifying behavior, and therefore the standard thermionic emission (TE) theory can be adapted

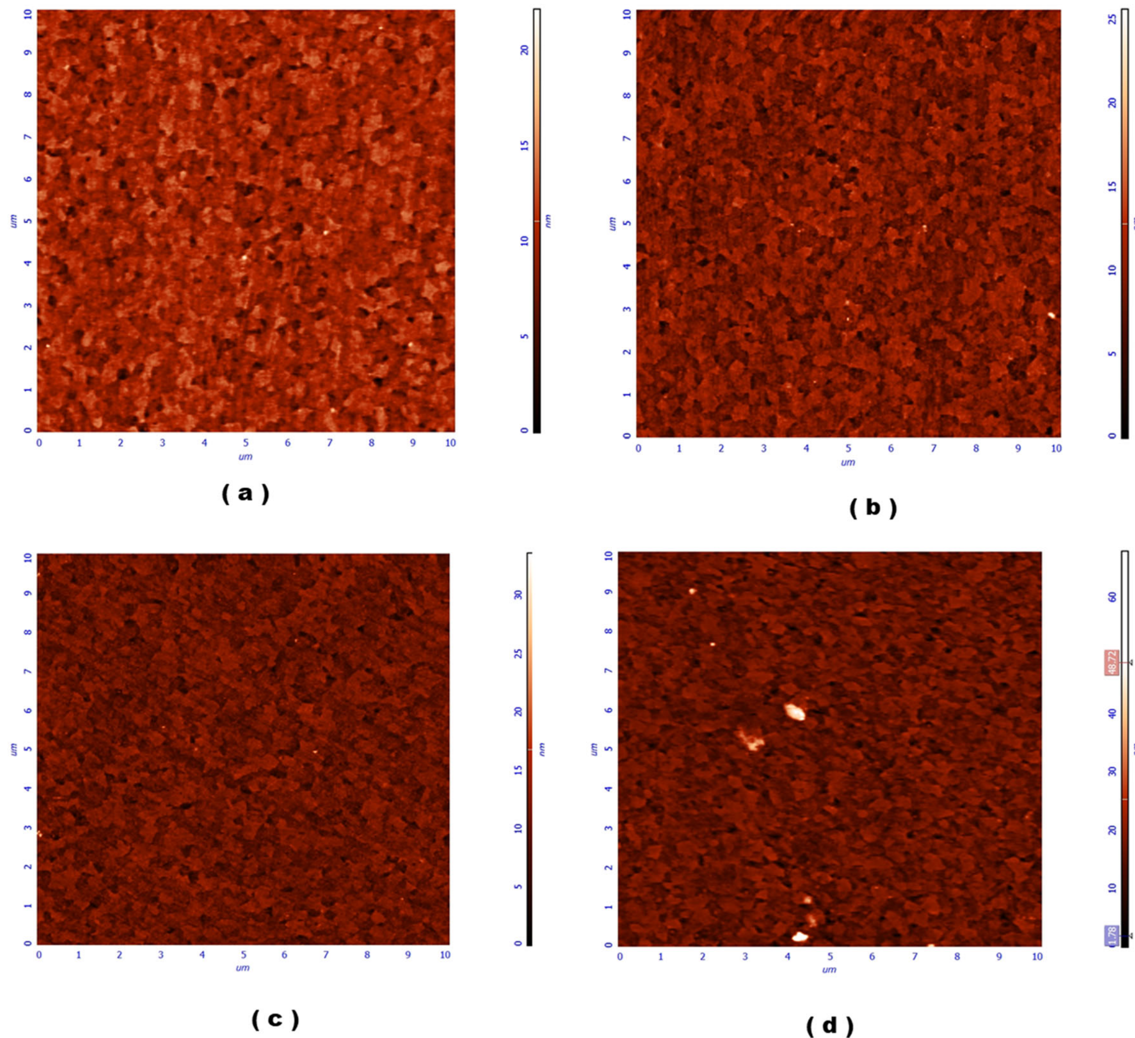

Fig. 4 AFM images of $[Zn(C_6H_6N_2O)_2(C_6H_4NO_2)_2(H_2O)]$ 1/2(H_2O) mixed ligand complex in different additive densities: **a** 0.5 mg Zn-complex, **b** 1 mg Zn-complex, **c** 2 mg Zn-complex and **d** 3 mg Zn-complex

to the analysis processes by the following $I-V$ relation [27, 47, 48].

$$I = I_0\left[\exp\left(\frac{qV}{nkT}\right) - 1\right] \quad (1)$$

where k is the Boltzmann constant, T is the temperature in Kelvin, q is the electronic charge and I_0 is the saturation current that related to the reverse current caused by the diffusion of minority charge carrier. I_0 can be defined by

$$I_0 = AA^*T^2\exp\left[-\frac{q\Phi_B}{kT}\right] \quad (2)$$

where A is the effective diode area and A^* is the effective Richardson constant (112 A/cm^2K^2 for the n-Si) [47].

When incident light comes into a photodiode, three types of photocurrent generating mechanisms are produced: (1) electrons are excited from the metal and injected into the semiconductor, (2) electron–hole pairs are produced within the depletion region of the semiconductor and (3) photodiode works in avalanche mode to generate photocurrent. The formation of these mechanisms depends on energies of the incident photons, applied bias and breakdown voltage of photodiode [49]. As shown in the corresponding figures, the current in the forward bias region increases with increasing light intensity. As light intensity increases, production of electron–hole pairs increases due to the absorption of light, and in turn, photocurrent of the diode increases. On the other hand, increase in photocurrent caused by

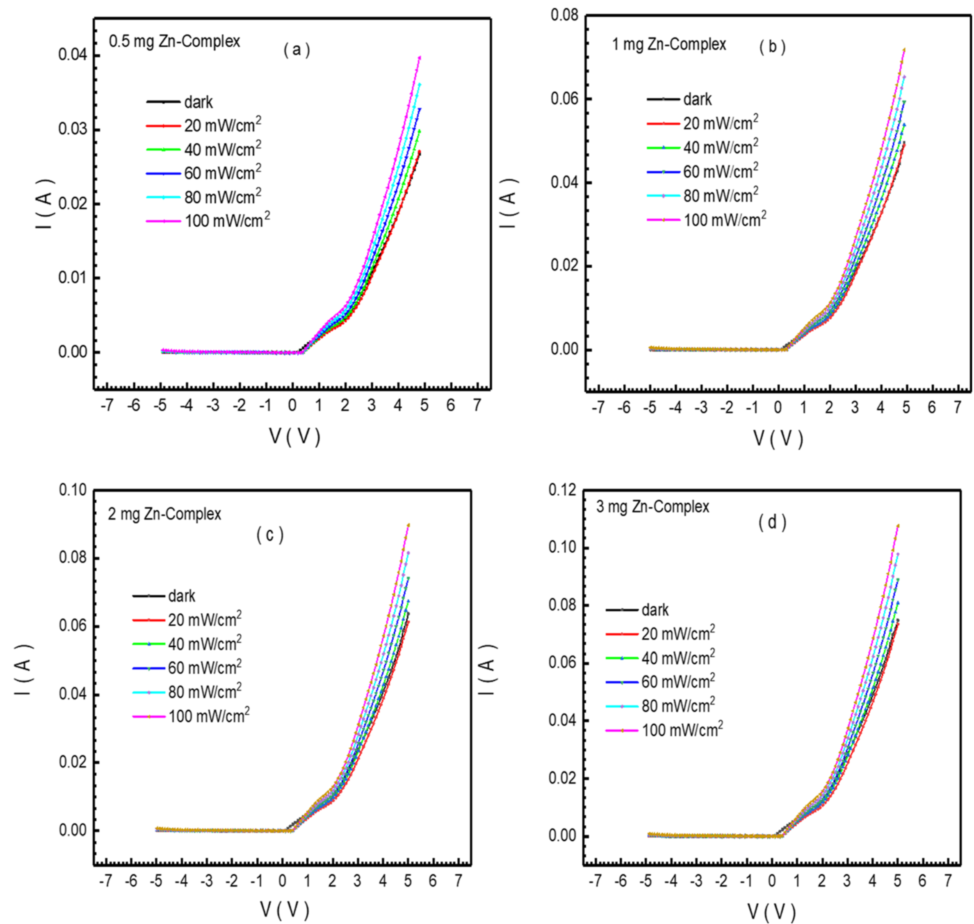

Fig. 5 Forward and reverse bias $I-V$ plots of Au/Zn-complex/n-Si/Au photodiodes in different additive densities: **a** 0.5 mg Zn-complex, **b** 1 mg Zn-complex, **c** 2 mg Zn-complex and **d** 3 mg Zn-complex

increase in the intensity of light can be associated with large number of incoming photons and the resulting large number of electron–hole pairs [50].

To compare the rectifying behavior of Au/Zn-complex/n-Si/Au MPS photodiodes depending on the Zn content, the semi-logarithmic $I-V$ characteristics are presented in Fig. 6a at 100 mW cm^{-2} illumination intensity. Due to the space charge layer formed in the interface region, the photodiodes exhibit good rectification properties [48]. The rectification factor (RF) (the ratio of forward current to the reverse current) of diodes for 0.5 mg Zn-complex, 1 mg Zn-complex, 2 mg Zn-complex and 3 mg Zn-complex content are obtained as 1.75×10^3, 1.87×10^3, 1.93×10^3, and 2.01×10^3, respectively, at $\pm$ 5 V. The Zn-complex contribution slightly increases photosensitive properties of the photodiodes with increasing the current values from 1.42×10^{-5} to 4.11×10^{-5} A. The results show that response of the fabricated photodiodes to illumination is affected by the amount of Zn mass and thus, the photodiode with 3 mg Zn-complex is found to be in the best photocurrent contribution. This can be attributed to the fact that Zn-complex mass acts as a donor by settling in a cation position and consequently it increases the carrier concentration [51, 52].

Figure 6b shows the semi-logarithmic $I-V$ plots of Au/3 mg Zn-complex/n-Si/Au MPS photodiode under dark and distinct light intensities. As given in this figure, currents in the reverse bias direction increase more clearly compared to currents in the forward direction, depending on illumination intensity. Significant difference between dark and illuminated currents is obtained in the reverse bias region. This behavior under illumination indicates that the fabricated diodes carry a photodiode property. Moreover, an increasing current is observed with increasing illumination intensity in the reverse bias region. This type of behavior also supports photosensitive behaviors of the diode. The values of n and I_0 are calculated as 3.22 and 3.88×10^{-5}A from slope and intercept of straightline region of semi-logarithmic $I-V$ plots (Fig. 6b), respectively, under dark environment. In literature, conventional Au/n-Si MS

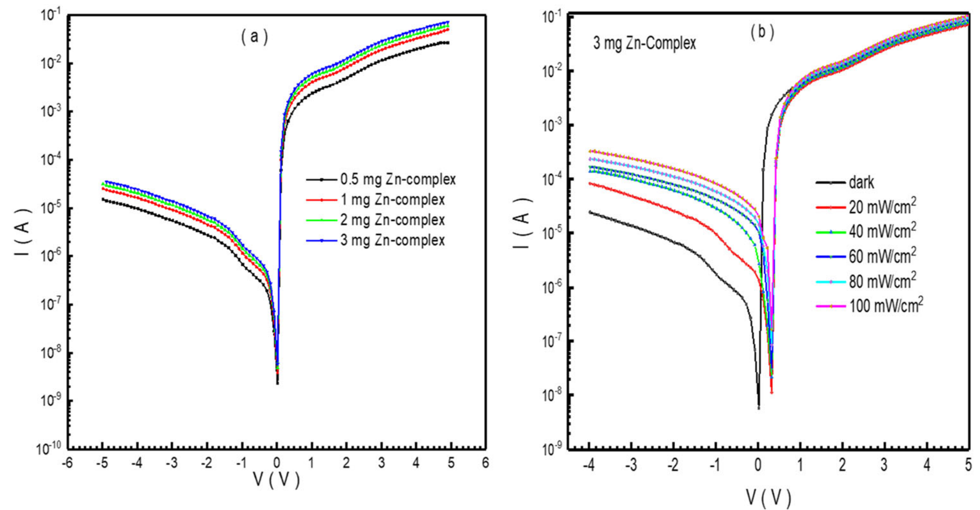

Fig. 6 Forward and reverse semi-logarithmic $I-V$ curves of Au/Zn-complex/n-Si/Au photodiode: **a** with various masses and **b** for 3 mg Zn-complex under distinct light intensity

diode gives lower n values around 1.03–1.69 compared to the polymeric interface layer contributed diode [53–58]. These high value for MIS type diode can be explained by intentionally deposited Zn-complex layer at the junction interface and therefore change in interface states and formation of barrier height at the interface region [59]. On the other hand, the reason for high n can be attributed to spatial distribution of interface states, tunneling current of the semiconductor and regeneration-recombination effects [27, 47, 48]. Using the obtained I_0 value, Φ_B is calculated as 0.571 eV with the help of Eq. (2). On the other hand, the forward photocurrent is found to be 1.2×10^{-2} A at 2 V from $\ln I-V$ curves (Fig. 6b) under 20mW/cm^2 illumination. Dokme et al. report the forward photocurrent about 8.5×10^{-3} A at room temperature using $\ln I-V$ measurements for a similar polymeric structure type (Au/PVA(Co, Zn-Doped)/n-Si) under 20 mW/cm^2 [58]. Similarly, Altindal et al. report the forward photocurrent about 7.5×10^{-3} A at 2 V for Au/PVA(Ni, Zn-doped)/n-Si under 25 mW/cm^2 [60]. From the obtained device performance results, it is seen that the nicotinate/nicotinamide mixed ligand complex produces a higher photocurrent than its counterparts and constitutes an alternative to PVA polymer composite materials, which are of great interest in electronic device fabrications.

Series resistance (R_s) values of Au/Zn-complex/n-Si/Au photodiodes are obtained by using Cheung's functions [61] as:

$$\frac{dV}{d(\ln I)} = n\frac{kT}{q} + IR_s \quad (3)$$

$$H(I) = V - \left(\frac{nkT}{q}\right)\ln\left(\frac{I}{AA^*T^2}\right) \quad (4)$$

$$H(I) = n\Phi_B + R_sI \quad (5)$$

In Fig. 7, experimental $dV/d(\ln I)$ versus I and $H(I)$ versus I (inset) plots depending on Zn contents are presented for Au/Zn-complex/n-Si/Au photodiodes. Equation (3) indicates a straightline for the curvature region of the forward bias $I-V$ curves, thus, R_s values can be obtained from slope of $dV/d(\ln I)$ versus I curves. $H(I)$ versus I plots also give a straight line for the curvature region of the

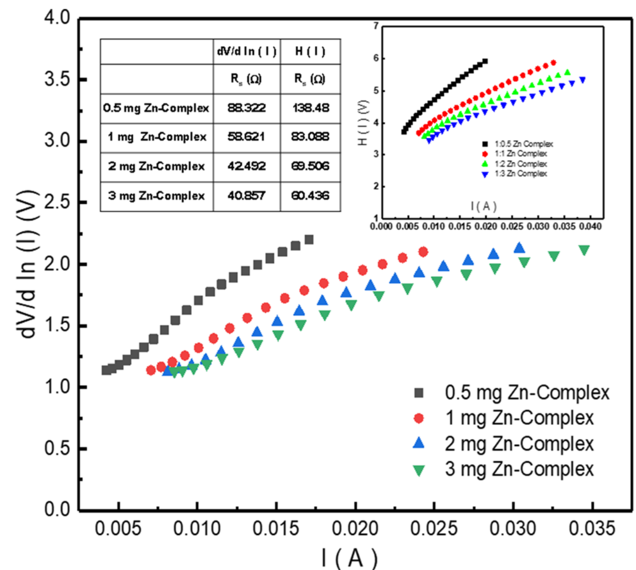

	dV/d ln (I)	H (I)
	R_s (Ω)	R_s (Ω)
0.5 mg Zn-Complex	88.322	138.48
1 mg Zn-Complex	58.621	83.088
2 mg Zn-Complex	42.492	69.506
3 mg Zn-Complex	40.857	60.436

Fig. 7 $dV/d(\ln I)$ versus I and $H(I)$ versus I (inset) plots of Au/Zn-complex/n-Si/Au photodiode for 0.5, 1, 2, and 3 mg Zn-complexes

forward bias $I-V$ characteristics (as shown in the inset of Fig. 7). Therefore, slope of this plot also provides an additional determination way of R_s. R_s values of the photodiodes are obtained as 40–50 Ω for 3 mg Zn-complex content and tabulated for other Zn dopant amounts in Fig. 7. According to the base MS diode, this value is around 1.93–6.70 kΩ derived from direct relation between current and voltage using Ohm's law and Cheung's method [53, 56]. Dokme et al. [58] and Altindal et al. [60] report R_s values as 276.11 and 99.71Ω under dark; and 116.14 and 82.56 Ω under illuminated environment, respectively, for same type of structures at room temperature by using Cheung's method. On the other hand, these are lower than resistance in MS diode where these results can be examined under the possible effect of variation in experimental conditions.

Figure 8 shows variation of the photocurrent with illumination intensity at various doping levels. photocurrent nature of the diodes is analyzed by the following relationship [61, 62].

$$I_{ph} = CP^m \quad (6)$$

where I_{ph} is photocurrent produced in the diode by solar illumination, P is intensity of lighting on the diode, m is lighting coefficient and C is proportional constant of relationship between I_{ph} and P. As seen in Fig. 8, I_{ph} values increase with increasing the lighting intensities. The obtained straight line represents a linear photoconductivity behavior of all fabricated devices and the increment of photoconductive sensitivity is due to the excitation of electron–hole pairs by incident light [63]. This photoconduction mechanism occurred in the diode can be clarified by the value of m, which is related to photocarriers lifetime. If this value is between 0 and 1, lifetime of photocarriers is defect controlled. Namely, they can be found under dominant effect of trap centers [64]. On the other hand, if $m = 1$, monomolecular recombination becomes dominant. The higher values occur due to low intensity unobstructed trap levels [65]. Among the fabricated diodes, the device with 3 mg Zn-complex provides the highest photoconductivity. This can be attributed to increasing number of charge carriers with increasing Zn-complex mass [51, 52]. It can be observed from Fig. 8 that the photocurrent is increased from 7.37×10^{-2} to 1.11×10^{-1} A with increase in light intensity for 3 mg Zn-complex/n-Si diode. This fact shows reaction of electrons in the valance band to jump to the conduction band with the energy received from the incident light [66]. The values of m is found from slope of the plots (in Fig. 8) as to be 0.51, 0.56, 0.53, and 0.54 for 0.5 mg Zn-complex/n-Si, 1 mg Zn-complex/n-Si, 2 mg Zn-complex/n-Si and 3 mg Zn-complex/n-Si diodes, respectively. These values are in $0 < m < 1$ interval and it can be concluded that the localized state distribution continuously exists at the interface [67, 68].

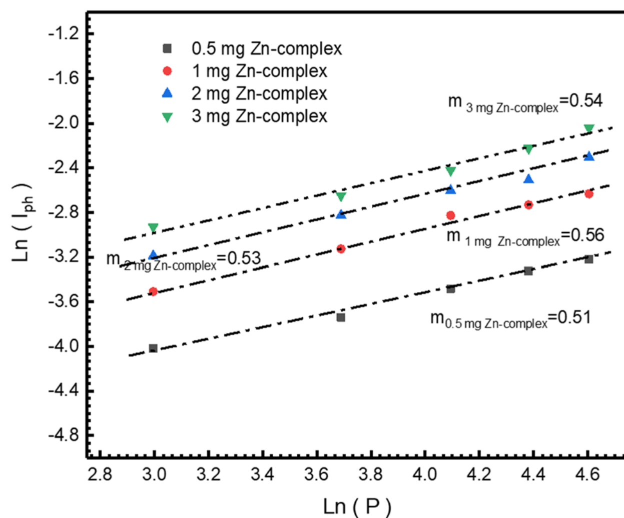

Fig. 8 Variation of the photocurrent with illumination intensity depending on different Zn-complex mass

In order to discuss the photoconductivity mechanism, it is more convenient to make reaction time measurements in addition to evaluation of the photocurrent variations. In Fig. 9a–d, current transient graphs of the photodiodes depending on the various doping ratio of Zn are displayed for 20, 40, 60, 80 and 100 mW/cm^2 light-power densities at applied − 3 V bias. Photocurrent transient measurements is a well-known technique to understand the photoconduction mechanism and to show the photoresponse properties for various power densities during the device on and off positions [8, 69]. When illumination is turned on, number of free charge carriers increase and they contribute to the current flow and photocurrent values quickly reach a saturation level. When it is turned off, charge carriers are trapped at lower levels and photocurrent drops rapidly to its initial level [70, 71]. This case represents a reversible switching behavior of the devices [72]. As can be seen from Fig. 9a–d, the devices show a good stability and fast photoresponse under distinct illumination intensity for all doping levels and they reach to the maximum value of I_{ph} in

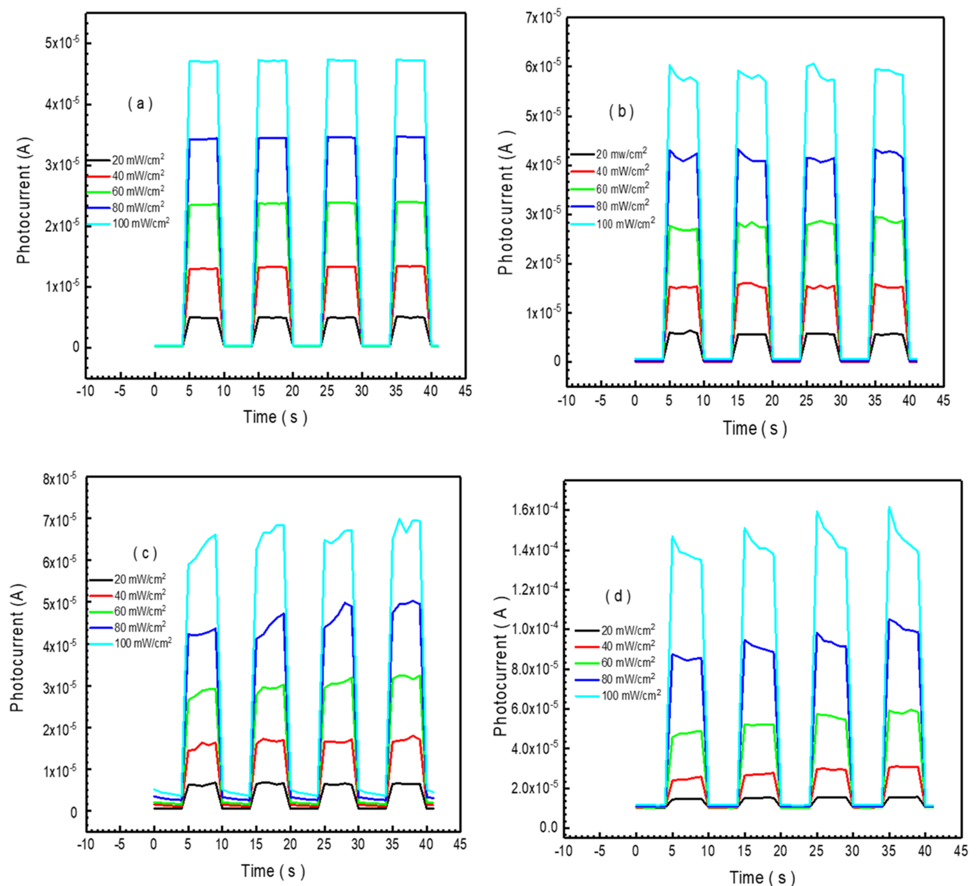

Fig. 9 Current transient graphs depending on the various masses: **a** 0.5 mg Zn-complex, **b** 1 mg Zn-complex, **c** 2 mg Zn-complex and **d** 3 mg Zn-complex

about a second. In the case for the sample of 0.5 mg Zn-complex, the photocurrent increases from 3.13×10^{-7} to 4.68×10^{-5} A under 100 mW/cm^2 illumination, and then it drops to 5.85×10^{-7} A after turning off illumination. This result clearly indicates that the fabricated device exhibits a photoconductive behavior. Initial rise of the current indicates generation mechanism of free charge carriers. Decay of the current indicates trapping mechanism of the charge carriers in deep levels after turning off illumination. Moreover, the photocurrent of diodes increases with increasing the doping ratio. This type of behavior can be attributed to the surface properties of device that consist of stratified [73].

In order to understand the performance parameters of the photodiodes, $C-V$ and $G-V$ measurements are carried out as a function of applied bias for various Zn doping ratios (Fig. 10). As seen from these plots, both the capacitance and conductance values of the diodes are affected by the forward applied bias. $C-V$ plots exhibit peaks in the low forward bias region and the value of capacitance decreases toward high biases. The observed peaks can be attributed to the rearrangement of interface states in regions near the middle of the band gap [74]. It is seen from Fig. 10a, these values of photodiodes are increased with increasing doping levels. This indicates that the contribution of Zn supports the interfacial states in these photodiodes [73]. On the other hand, the highest conductivity is measured for 3 mg Zn-complex (Fig. 10b).

In addition to these measurements, electrical characteristics of the photodiodes are detailed with these analyses at different frequencies. Figure 11a and b present the frequency dependence of these plots for 3 mg Zn-complex/n-Si diode. As presented in Fig. 11a, the values of capacitance decrease with increasing frequency. These capacitive characteristics indicate the existence of an inhomogeneous layer due to the presence of interface states that acts in a series with the insulator capacitance and causes a frequency distribution [75]. This also results in the space charge formation at interface to follow the ac signal at low frequencies and contribute to the capacitance values depending on frequency [76]. However, for sufficiently high frequencies ($f \geq$ 500 kHz), the interface

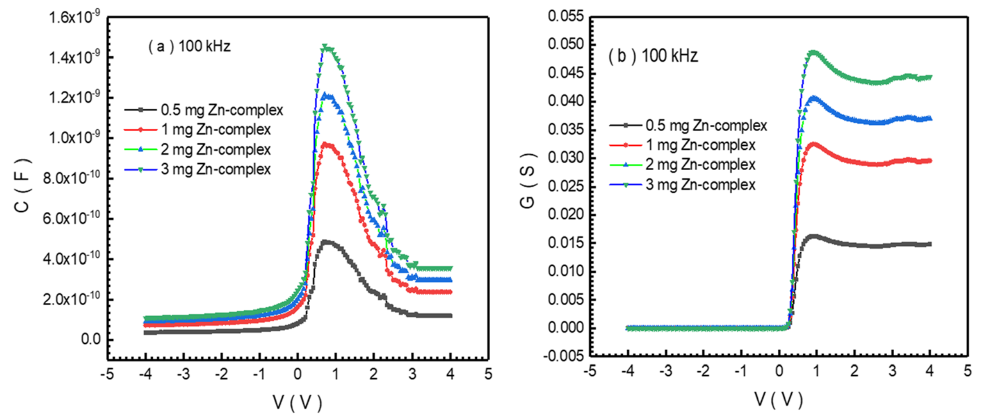

Fig. 10 **a** $C-V$ and **b** $G-V$ characteristics depending on the various Zn-complex masses

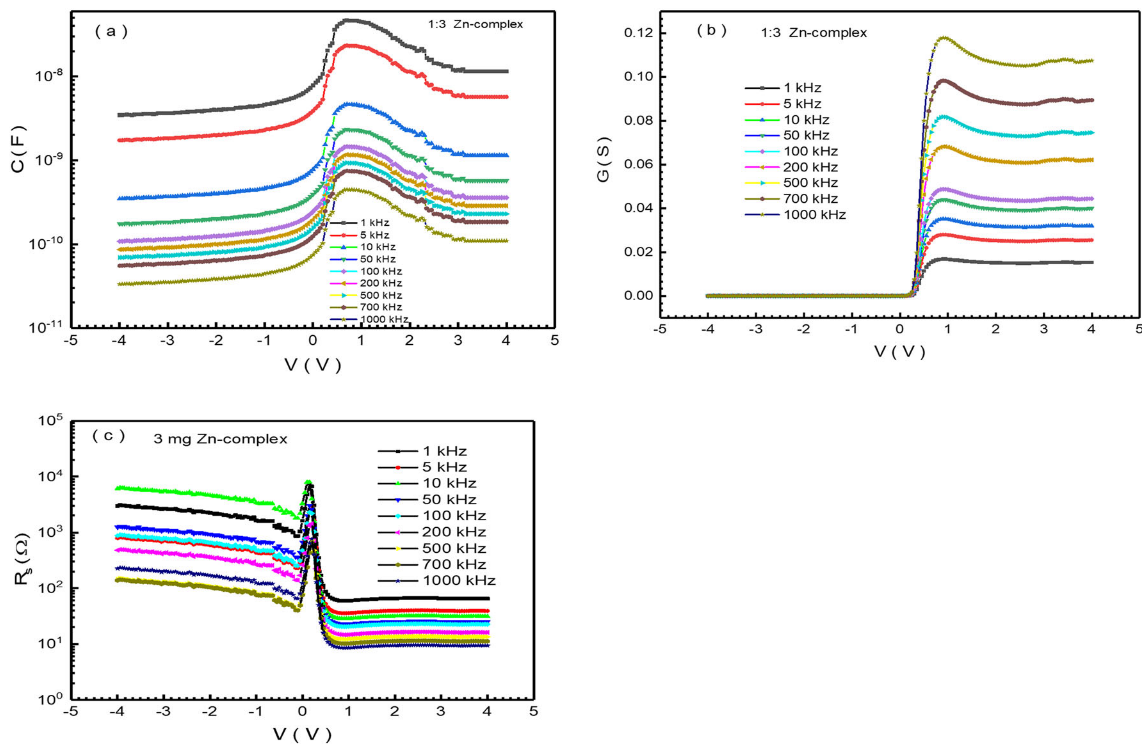

Fig. 11 Frequency dependence of the **a** $C-V$, **b** $G-V$ and **c** R_s-V plots for 3 mg Zn-complex/n-Si diode

states cannot be able to follow AC signal. As a result of this situation, contribution of the interface states to the total capacitance can be assumed as to be negligibly small [77]. As shown from Fig. 11a, the responses to both applied bias and frequency are observed in the forward bias region. Moreover, in the reverse bias region, the diodes do not give a remarkable capacitance response at each voltage step and frequency.

Figure 11b presents the conductance values vs applied bias at various frequencies. As shown in this figure, the conductance values exhibit an increasing behavior with increasing frequency in the forward bias region. On the other hand, an abnormal peak is observed at all curves for each frequency in the forward bias region. This diode response can be attributed to presence of the natural interface layer, interface states in the active region, and R_s [78].

The R_s values of a Schottky diode with an interfacial layer can be obtained using the measured capacitance and conductance data in strong accumulation region at high frequencies [6, 7, 79]. At sufficiently high frequencies, when the diode with an

interfacial layer is held in a strong accumulation, the admittance (Y_{acc}) is given by [79],

$$Y_{acc} = G_{acc} + jwC_{acc} \quad (7)$$

where w is the angular frequency. G_{acc} and C_{acc} terms are the experimental values of conductance and capacitance in strong accumulation zone, respectively. Using the real and imaginary parts of the admittance expression, the series resistance of the Schottky diode with an interfacial layer is given as [79],

$$R_s = \frac{G_{acc}}{G_{acc}^2 + w^2 C_{acc}^2} \quad (8)$$

The obtained R_s values as a function of applied bias in the frequency range from 1 to 1000 kHz are plotted in Fig. 11c for 3 mg Zn-complex. As given in Fig. 11c, the R_s values give sharp peaks depending on the frequency in the voltage range of 0–1 V. The reason for change in these values with changing frequency is due to the mobile and trapped interfacial charges [80, 81]. Moreover, there is a strong response in these graphs in the reverse bias region. This is trapped charge effect due to both voltage and frequency variation, and it can be attributed to inhomogeneity of the interface distribution [82].

The adjusted capacitance (C_{adj}) and equivalent parallel conductance (G_{adj}) values can be analyzed by discarding the effects of R_s as [83],

$$C_{adj} = \frac{\left[G_m^2 + (wC_m)^2\right] C_m}{a^2 + (wC_m)^2} \quad (9)$$

and

$$G_{adj} = \frac{\left[G_m^2 + (wC_m)^2\right] a}{a^2 + (wC_m)^2} \quad (10)$$

In these relations, a is given as follows:

$$a = G_m - \left[G_m^2 + (wC_m)^2\right] R_s \quad (11)$$

where C_m and G_m are the measured capacitance and conductance values, respectively. Using these equations, the C_{adj} and G_{adj} values as a function of applied bias are given in Fig. 12a and b, respectively, in the frequency range from 1 to 1000 kHz for 3 mg Zn-complex/n-Si diode. In these calculations, the resistance value in the accumulation region is used for each frequency value. As seen from Fig. 12a and b, a decrease is observed in the capacitance and

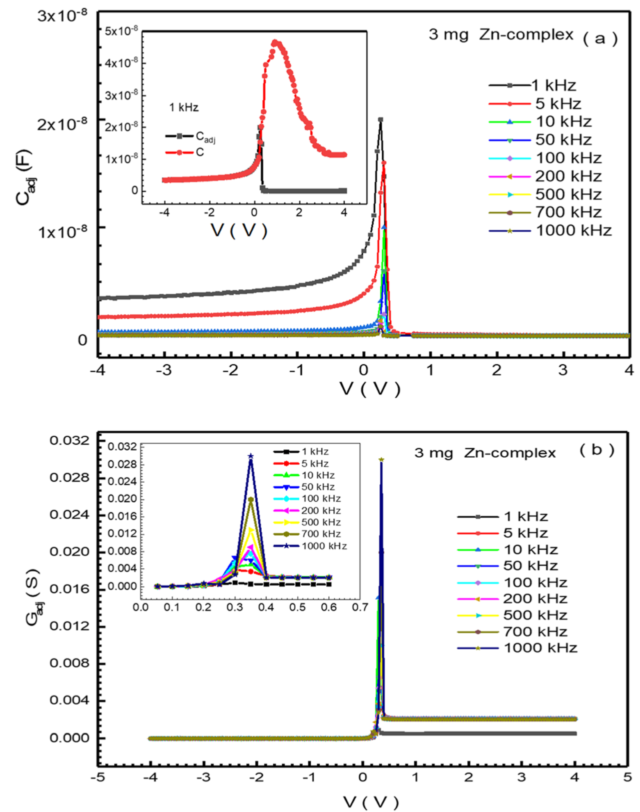

Fig. 12 Adjusted **a** $C-V$ plots under various frequencies while the insets represent the plots at 1 kHz. and **b** $G-V$ under various frequencies while the insets represent the $G-V$ plots in the voltage range 0–0.6 V

conductance values. Namely, the unadjusted capacitance peak value of 4.26×10^{-8} F ($\sim$ 1 V) is 2.13 times greater than the adjusted capacitance peak value of 2×10^{-8} F ($\sim$ 0.25 V), and the C_{adj} peak value of 3×10^{-2} S is 0.25 times smaller than the unadjusted conductance value of 1.17×10^{-1} S at 1000 kHz. Although a decreasing tendency is expected in the C_{adj} and G_{adj} values, it is impossible to eliminate the resistance effects [84, 85]. It is seen from the figures, the peak on the adjusted $G-V$ curves means there is no reduction in the effect of R_s [84]. In both cases, the distribution of interface states between the metal and semiconductor are the factors that govern electrical properties of the device [85].

The transient photocapacitance (C_{ph}) and photoconductance (G_{ph}) measurements are carried out as a function of time (Fig. 13) to detail effects of photogenerated carriers depending on Zn doping levels. As seen from both figures, photocapacitance and photoconductivity of the diodes are detected due to photogenerated carriers [86, 87]. The photocapacity

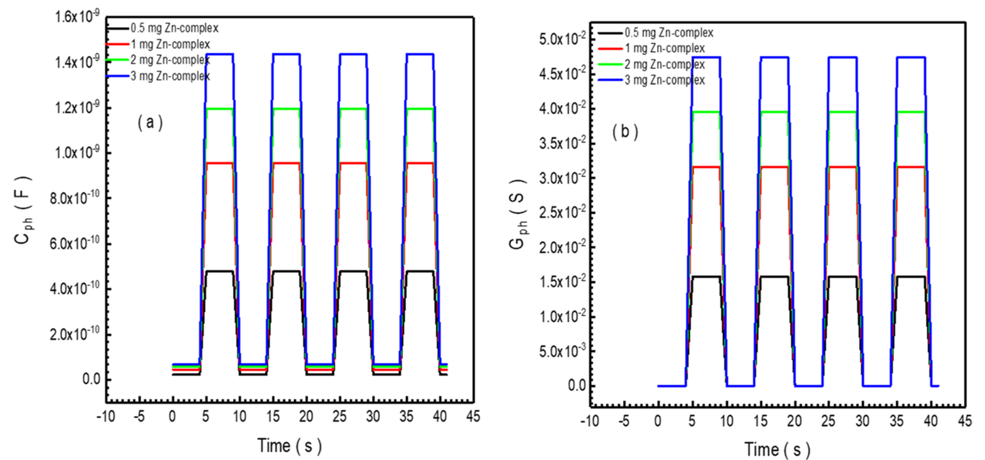

Fig. 13 Transient C_{ph} (**a**) and G_{ph} (**b**) plots as a function of time depending on various Zn-complex masses

consists of photogenic charges at the interface of the diodes. In addition, a strong dependence of lighting intensity of C_{ph} and G_{ph} values are observed for all Zn contributions. During the illumination, the produced carriers contribute to the conduction process by increasing C_{ph} and G_{ph} values up to certain values [62, 64]. Moreover, when the intensity of illumination is increased, these values increase and reach to the highest level. After the lighting is switched off, C_{ph} and G_{ph} values decrease and return to their initial values due to the trapped charge carriers in deep levels. Regarding to Fig. 13a and b, both C_{ph} and G_{ph} values increase with increasing Zn doping levels. It also can be seen from Fig. 13b, the highest photoconductivity for 3 mg Zn-complex is measured around 4.75×10^{-2} S while the highest photoconductivity measured for 0.5 mg Zn-complex has the value of 1.56×10^{-2} S. These results confirm that Zn-complex contribution enhance the photosensitivity and consequently the fabricated Schottky diodes have a potential as a type of light-responsive diode.

4 Conclusion

In this study, a metal-doped $[Zn(C_6H_6N_2O)_2(C_6H_4NO_2)_2(H_2O)]\cdot 1/2(H_2O)$ complex interlayered MPS diode structure is presented with the analyses of its diode behavior under dark and illumination. For this, a metal-nicotinate/nicotinamide mixed ligand complex is synthesized with distinct Zn mass as an interfacial layer to fabricate the photodiodes. The electrical measurements performed under different light intensities reveal that all fabricated structures are sensitive to the light and exhibit good rectifying behavior. In addition, the amount of Zn dopant in complex improves opto-electronic properties of the structure and provides a better photoconductive behavior in the diodes. According to these results, it is found that the Au/Zn-complex/n-Si/Au device can be candidate for use in many opto-electronic applications as a photoresponsive device.

Author contributions

Conceptualization: [SK, DEY, HHG]; Methodology: [DEY]; Investigation: [DAK, AAH, MY]; Resources [DAK, DEY]; Writing—original draft preparation: [SK, DEY, HHG]; Supervision: [DEY].

Data availability

The datasets generated during and/or analyzed during the current study are available from the corresponding author on reasonable request.

Declarations

Conflict of interest The authors declare that there are no conflicts of interest regarding the publication of this paper.

References

1. S. Chand, S. Bala, Appl. Surf. Sci. **252**, 358–363 (2005)
2. H. Simchi, M. Heidarisaani, M. Esmaeilzadeh, AIP Adv. **3**, 032124 (2013)

3. P. Xia, X. Feng, R.J. Ng, S. Wang, D. Chi, C. Li, Z. He, X. Liu, K.-W. Ang, Sci. Rep. **7**, 40669 (2017)
4. K. Ejderha, S. Duman, C. Nuhoglu, F. Urhan, A. Turut, J. Appl. Phys. **116**, 234503 (2014)
5. I. Jyothi, V. Janardhanam, H. Hong, C.J. Choi, Mater. Sci. Semicond. Process. **39**, 390–399 (2015)
6. D.E. Yildiz, S. Altindal, Z. Tekeli, M. Ozer, Mater. Sci. Semicond. Process. **13**, 34–40 (2010)
7. E. Yenel, Y. Torlak, A. Kocyigit, I. Erden, M. Kus, M. Yildirim, J. Mater. Sci.: Mater. Elecron. **32**, 12094–12110 (2021)
8. B.A. Gozeh, A. Karabulut, A. Yildiz, F. Yakuphanoglu, J. Alloys Compd. **732**, 16–34 (2018)
9. O. Cicek, H.U. Tecimer, S.O. Tan, H. Tecimer, S. Altindal, I. Uslu, Compos. B Eng. **98**, 260–268 (2016)
10. G. Ersoz, I. Yucedag, Y. Azizian-Kalandaragh, I. Orak, S. Altindal, IEEE Trans. Electron. Devices **63**, 2948–2955 (2016)
11. L. Beecroft, C.K. Ober, Chem. Mater. **9**, 1302 (1997)
12. C. Zhang, S. Hoger, K. Pakbaz, F. Wudl, A.J. Heeger, J. Electron. Mater. **23**, 453–458 (1994)
13. C. Cetinkaya, E. Cokduygulular, B. Kinaci, F. Guzelcimen, I. Candan, H.I. Efkere, Y. Ozen, S. Ozcelik, Opt. Mater. **120**, 111457 (2021)
14. D.E. Yildiz, D.H. Apaydın, L. Toppare, A. Cirpan, J. Ploym. Sci. **128**, 1659–1664 (2013)
15. S.S. Li, Y.Y. Lin, W.F. Su, C.W. Chen, IEEE J. Sel. Topics Quantum Electron. **16**, 1635–1640 (2010)
16. V. Tamilavan, P. Sakthivel, Y. Li, M. Song, C.H. Kim, S.H. Jin, M.H. Hyu, J. Polym. Sci. A Polym. Chem. **48**, 3169–3177 (2010)
17. S. Demirezen, I. Orak, Y. Azizian-Kalandaragh, S. Altindal, J. Mater. Sci.: Mater. Electron. **28**, 12967–12976 (2017)
18. M.S.P. Reddy, H.S. Kang, J.H. Lee, V.R. Reddy, J.S. Jang, J. Appl. Polym. Sci. **131**, 39773 (2014)
19. C. Tozlu, A. Mutlu, Synth. Met. **211**, 99–106 (2016)
20. N. Matsuki, Y. Irokawa, Y. Nakano, M. Sumiya, Sol. Energy Mater. Sol. Cell **95**, 284–287 (2011)
21. H.A. Bioki, Appl. Phys. **62**, 20210 (2013)
22. V.C. Nguyen, K.P. Kamloth, Thin Solid Films **338**, 142–148 (1999)
23. P.S. Abthagir, R. Saraswathi, J. Appl. Polym. Sci. **81**, 2127–2135 (2001)
24. H. Tecimer, S.O. Tan, S. Altindal, IEEE Trans. Electron. Devices **65**, 231–236 (2018)
25. I. Dokme, D.E. Yildiz, S. Altindal, Adv. Polym. Technol. **31**, 63–70 (2012)
26. H.C. Card, E.H. Rhoderick, J. Phys. D Appl. Phys. **4**, 1589–1601 (1971)
27. S.M. Sze, *Physics of Semiconductor Devices* (Wiley, New York, 1981)
28. D.E. Yildiz, H.H. Gullu, L. Toppare, A. Cirpan, J. Mater. Sci.: Mater. Elecron. **31**, 15233–15242 (2020)
29. H.H. Gullu, D.E. Yıldız, L. Toppare, A. Cirpan, J. Mater. Sci.: Mater. Electron. **31**, 18816–18831 (2020)
30. H. Dogan, I. Orak, N. Yildirim, Sci. J. (CSJ) **38**, 329–341 (2017)
31. L. Rajan, C. Periasamy, V. Sahula, IEEE Trans. Nanotechnol. **15**, 201–208 (2016)
32. H.G. Cetinkaya, D.E. Yildiz, S. Altindal, Int. J. Mod. Phys. B **29**, 1450237–1450315 (2015)
33. I. Candan, Y. Ozen, Poym. Bull. **78**, 3117–3129 (2021)
34. A.S. Dahlan, A. Tatarolu, A.A. Al-Ghamdi, A.A. Al-Ghamdi, S. Bin-Omran, Y. Al-Turki, F. El-Tantawy, F. Yakuphanoglu, J. Alloys Compd. **646**, 1151–1156 (2015)
35. A. Mekki, R.O. Ocaya, A. Dere, A.A. Al-Ghamdi, K. Harrabi, F. Yakuphanoglu, Synth. Met. **213**, 47–56 (2016)
36. O.S. Cifci, M. Bakir, J.L. Meyer, A. Kocyigit, Mater. Sci. Semicond. Process. **74**, 175–182 (2018)
37. Y. Zhao, K. Zhu, J. Phys. Chem. C **118**, 9412–9418 (2014)
38. F. Yigiterol, H.H. Gullu, O. Bayrakli, D.E. Yildiz, J. Electron. Mater. **47**, 2979–2987 (2018)
39. A. Mekki, A. Dere, K. Mensah-Darkwa, A. Al-Ghamdi, R.K. Gupta, K. Harrabi, W.A. Farooq, F. El-Tantawy, F. Yakuphanoglu, Synth. Met. **217**, 43–56 (2016)
40. N.A. Unlu, S.O. Hacioglu, G. Hizalan, D.E. Yildiz, L. Toppare, A. Cirpan, J. Electrochem. Soc. **164**, G71–G76 (2017)
41. H.H. Gullu, D.E. Yildiz, A. Kocyigit, M. Yıldırım, J. Alloys Compd. **827**, 154279 (2020)
42. Y. Ozen, I. Candan, Chem. Phys. Lett. **740**, 137078 (2020)
43. D.A. Kose, H. Necefoglu, O. Sahin, O. Buyukgungor, J. Therm. Anal. Calorim. **110**, 1233–1241 (2012)
44. D.A. Kose, F. Akkurt, O. Sahin, O. Buyukgungor, J. Chin. Chem. Soc. **61**, 1326–1332 (2014)
45. O. Dagli, D.A. Kose, O. Sahin, Z.S. Sahin, J. Therm. Anal. Calorim. **127**, 1373–1383 (2017)
46. E.H. Rhoderick, R.H. Williams, *Metal-Semiconductor Contacts* (Clarendon Press, Oxford, 1988)
47. H.H. Gullu, D.E. Yildiz, J. Mater. Sci.: Mater. Electron. **30**, 19383–19394 (2019)
48. M.A. Hassan, J. Al-Nahrain, J. Sci. **15**, 73–79 (2012)
49. S.S. Li, *Semiconductor Physical Electronics* (Springer, New York, 2006)
50. Z. Ahmad, M.H. Sayyad, M. Yaseen, M. Ali, Eng. Technol. **52**, 811–814 (2011)
51. S. Ruzgar, M. Caglar, Mater. Sci. Semicond. Process. **115**, 105076 (2020)
52. A. Turut, D.E. Yildiz, A. Karabulut, I. Orak, J. Mater. Sci.: Mater. Electron. **31**, 7839–7849 (2020)
53. M. Gokcen, S. Altindal, M. Karaman, U. Aydemir, Physica B **406**, 4119–4123 (2011)

54. I. Tascioglu, U. Aydemir, S. Altindal, J. Appl. Phys. **108**, 064506 (2010)
55. E. Ugurel, S. Aydogan, K. Serifoglu, A. Turut, Microelectron. Eng. **85**, 2299–2303 (2008)
56. A.G. Imer, E. Kaya, A. Dere, A.G. Al-Sehemi, A.A. Al-Ghamdi, A. Karabulut, F. Yakuphanoglu, J. Mater. Sci. Mater. Electron. **31**, 14665–14673 (2020)
57. F. Yakuphanoglu, Microelectron. Eng. **87**, 1884–1888 (2010)
58. I. Dokme, S. Altindal, I. Uslu, J. Appl. Polym. Sci. **125**, 1185–1192 (2021)
59. M.A.M. Hassan, A.F. Saleh, S.J. Mezher, Appl. Nanosci. **4**, 695–701 (2014)
60. S. Altindal, T. Tunc, H. Tecimer, I. Yucedag, Mater. Sci. Semicond. Process. **28**, 48–53 (2014)
61. S.K. Cheung, N.W. Cheung, Appl. Phys. Lett. **49**, 85 (1986)
62. A. Karabulut, A. Dere, A.G. El-Sehemi, A.A. Al-Ghamdi, F. Yakuphanoglu, Electron. Mater. **47**, 7159–7169 (2018)
63. Y.J. Lin, Y.M. Chin, H.C. Chang, ECS J. Solid State Sci. Technol. **6**, M5–M8 (2017)
64. D.E. Yildiz, H.H. Gullu, A. Sarilmaz, F. Ozel, A. Kocyigit, M. Yildirim, J. Mater. Sci.: Mater. Electron. **31**, 935–948 (2020)
65. M. Soylu, A.A. Al-Ghamdi, F. Yakuphanoglu, Microelectron. Eng. **99**, 50–57 (2012)
66. D.E. Yıldız, A. Karabulut, I. Orak, A. Turut, J. Mater. Sci.: Mater. Electron. **32**, 10209–10223 (2021)
67. M. Cavas, A.A.M. Farag, Z.A. Alahmed, F. Yakuphanoglu, J. Electroceram. **31**, 298–308 (2013)
68. R.K. Gupta, A.A. Hendi, M. Cavas, A.A. Al-Ghamdi, O.A. Al-Hartomy, R.H. Aloraini, F. El-Tantawy, F. Yakuphanoglu, Phys. E **56**, 288–295 (2014)
69. A.S. Dahlan, A. Tataroglu, A.A. Al-Ghamdi, A.A. Al-Ghamdi, S. Bin-Omran, Y. Al-Turki, F. El-Tantawy, F. Yakuphanoglu, J. Alloys Compds. **646**, 1151–1156 (2015)
70. R.H. Bube, *Photoconductivity of Solids* (Wiley, New York, 1960)
71. F. Aslan, H. Esen, F. Yakuphanoglu, Optik **197**, 163203 (2019)
72. S. Dugan, M.M. Koc, B. Coskun, J. Mol. Sruct. **1202**, 127235 (2020)
73. A. Kocyigit, I. Orak, S. Aydogan, Z. Caldıran, A. Turut, J. Mater. Sci. Mater. Electron. **28**, 5880–5886 (2017)
74. W.L. Jeong, J.H. Min, H.S. Kim, I.Y. Kim, J.H. Kim, D.S. Lee, Thin Solid Films **638**, 305–311 (2017)
75. K. Prabakar, S.K. Narayandass, D. Mangalaraj, Phys. Status Solidi A **199**, 507–514 (2003)
76. D.E. Yıldız, J. Mater. Sci.: Mater. Electron. **29**, 17802–17808 (2018)
77. H.H. Gullu, D.E. Yildiz, J. Mater. Sci.: Mater. Electron. **32**, 13549–13567 (2021)
78. J.W. Jung, C.C. Chueh, A.K.Y. Jen, Adv. Mater. **27**, 7874–7880 (2015)
79. S. Ruzgar, S. Aksoy, Superlattice Microstruct. **145**, 106636 (2020)
80. A. Turut, Turk. J. Phys. **44**, 302–347 (2020)
81. B.L. Sharma, *Metal-Semiconductor Schottky Barrier Junctions and Their Applications* (Plenum Press, New York, 1984)
82. J.R. Brews, E.H. Nicollian, Solid State Electron. **27**(1984), 963–975 (1984)
83. D.E. Yıldız, H.K. Çavus, Surf. Rev. Lett. **24**, 1750077 (2017)
84. H.H. Gullu, D.E. Yildiz, O. Surucu, M. Parlak, J. Mater. Sci.: Mater. Electron. **31**, 9394–9407 (2020)
85. A. Dere, M. Soylu, F. Yakuphanoglu, Mater. Sci. Semicond. Process. **90**, 129–142 (2019)
86. S. Shukla, S. Kumar, Bull. Mater. Sci. **34**, 1351–1355 (2011)
87. F. Yakuphanoglu, K. Mensah-Darkwa, A.A. Al-Ghamdi, R.K. Gupta, W.A. Farooq, Microelectron. Eng. **160**, 27–33 (2016)

Publisher's Note Springer Nature remains neutral with regard to jurisdictional claims in published maps and institutional affiliations.